

To appear in The Astrophysical Journal. ©1998 The American  
Astronomical Society. All rights reserved.

## A Physical Model of Warped Galaxy Disks

Kimberly C. B. New<sup>1</sup>, Joel E. Tohline, Juhan Frank, and Horst M. V $\ddot{a}$ th<sup>2</sup>  
Department of Physics & Astronomy, Louisiana State University,  
Baton Rouge, LA 70803-4001

### ABSTRACT

Warped H I gas layers in the outer regions of spiral galaxies usually display a noticeably twisted structure. This structure almost certainly arises primarily as a result of differential precession in the H I disk as it settles toward a preferred orientation in an underlying dark halo potential well that is not spherically symmetric. In an attempt to better understand the structure and evolution of these twisted, warped disk structures, we have adopted the “twist–equation” formalism originally developed by Petterson (1977) to study accretion onto compact objects. Utilizing more recent treatments of this formalism, we have generalized the twist–equation to allow for the treatment of non–Keplerian disks and from it have derived a steady–state structure of twisted disks that develops from free precession in a nonspherical, logarithmic halo potential. We have used this steady–state solution to produce H I maps of five galaxies (M83, NGC 300, NGC 2841, NGC 5033, NGC5055), which match the general features of the observed maps of these galaxies quite well. In addition, the model provides an avenue through which the kinematical viscosity of the H I disk and the quadrupole distortion of the dark halo in each galaxy can be quantified. This generalized equation can also be used to examine the time-evolutionary behavior of warped galaxy disks.

*Subject headings:* galaxies: kinematics and dynamics — galaxies: structure — radio lines: galaxies

### 1. Introduction

In simplest terms, spiral galaxy disks can be described as geometrically thin, flat, and circular. We understand that spiral disks are geometrically thin because the gas of which they are composed

---

<sup>1</sup>Currently at the Department of Physics & Atmospheric Science, Drexel University, Philadelphia, PA 19104

<sup>2</sup>Currently at SAP AG, 69190 Walldorf, Germany

is cold (the sound speed of the gas is much smaller than its circular orbital velocity); and they are both circular and flat because, being dissipative, the gas is fairly efficient at both minimizing out-of-the-plane motions and radial excursions that would lead to departures from circular orbits.

Describing spiral disks as *perfectly* circular and flat is clearly an oversimplification, however. In addition to the nonaxisymmetric structures that are obvious in optical photographs of many spiral disks, 21-cm maps of the projected velocity fields of spiral disks often reveal isovelocity contours that are significantly twisted (Rogstad, Lockhart & Wright 1974; Reakes & Newton 1978; Rogstad, Crutcher & Chu 1979; Newton 1980a, 1980b; Bosma 1981; Schwarz 1985). Kinematical tilted-ring models have been constructed in an effort to explain the presence of such twists in the velocity maps of H I disks. The models indicate that the outer regions of many normal spiral disks are significantly warped out of the principal plane that is defined by the optically visible, central portion of each galaxy. The line of nodes that defines the intersection of adjacent rings of gas in these kinematical models also usually must be twisted significantly as a function of radius in order to explain the observed contour maps (for recent reviews, see Briggs 1990; Bosma 1991; Christodoulou, Tohline & Steiman-Cameron 1993, hereafter CTSC).

It is not particularly surprising that many galaxies are observed to possess extended, rotationally flattened disks because such structures appear to be fairly ubiquitous in gravitationally bound, astrophysical systems. (There is strong evidence, for example, that rotationally flattened disks either exist now or have existed in the past around our sun, individual planets within our solar system, numerous protostars, the primary star of many mass-exchanging binary star systems, and active galactic nuclei.) What is peculiar about the H I disks of many galaxies is that the disks are significantly warped. It is not clear why natural dissipative processes similar to those which work effectively to minimize out-of-the-plane motions in stellar or protostellar “accretion” disks are unable to suppress warps in the gaseous disks of galaxies. As Binney (1992) has reviewed, there still is no generally accepted dynamical model of spiral galaxies that satisfactorily explains either the origin or the current structure of warped H I disks.

Almost thirty years ago, Hunter & Toomre (1969) examined whether normal, infinitesimal bending oscillations might be exhibited by thin, rotating disks of self-gravitating material, permitting them to sustain coherent warps for more than a Hubble time. They concluded that “for any disk whose density tapers sufficiently gradually to zero near its edge,” the frequency spectrum of such oscillations is at least partly continuous and, as a result, coherent warps cannot be sustained. Over the subsequent decade, a number of other ideas surfaced to explain the persistence of warps in galaxies, each one taking advantage of the demonstrated existence of dark matter halos around galaxies. As Toomre (1983) has reviewed, however, models proposing to use the halo as an active agent to excite warps in otherwise flat disks – for example, via the Mathieu instability (Binney 1981) or via a flapping instability (Bertin & Mark 1980) – each present significant difficulties. Toomre (1983) and Dekel & Shlosman (1983) proposed, instead, that untwisted steady-state warps may be sustained as a result of steady forcing by a nonspherical, tilted halo. Building on the early work of Hunter & Toomre (1969) and the idea that forcing by a

nonspherical dark halo can influence the dynamics of the visible disks of galaxies, Sparke (1986) and Sparke & Casertano (1988) have shown that a discrete warping mode can persist if the disk is sufficiently self-gravitating and if it is embedded in a nonspherical halo whose equatorial plane is tilted with respect to the centralmost regions of the disk.

Adopting this model of galaxy warps, the following evolutionary picture emerges. During the galaxy formation process, gas which falls into a spheroidal dark matter halo generally will find that its angular momentum vector is tipped at some nonzero angle,  $i$ , away from the symmetry axis of the halo. If the gas is cold, it will settle into a rotationally flattened disk that is tilted at the same angle  $i$  with respect to the equatorial plane of the halo. In the centralmost regions of the galaxy, where the self-gravity of the gas (or, ultimately, the combined gas/star system) dominates over the gravitational influence of the halo, the gas will be content to remain in orbits that preserve this original tilt. In the outermost regions of the galaxy where the gravitational field of the halo dominates, however, the gas should settle into the halo’s equatorial plane. As Toomre (1983) and Dekel & Shlosman (1983) both sketched in their original concept papers, there also should be an intermediate region where the gas will be influenced significantly by the nonspherical gravitational fields of both the halo and the central gas (or gas/star) disk.

Through their modeling efforts, Sparke (1986) and Sparke & Casertano (1988) confirmed this earlier suspicion that in the intermediate region, the gas can reside in a steady-state, “warped disk” structure that provides a smooth radial transition between the separate “flat disk” orientations of the inner and outer regions of the galaxy. Concentrating on the dynamics of the centralmost and intermediate regions – that is, by building models in which there was effectively no gas in the outermost regions – Sparke & Casertano (1988) showed that, in steady-state, the warped disk exhibits a straight line of nodes which precesses slowly and coherently in a direction retrograde to the orbital motion of the gas. In a time-dependent simulation, furthermore, Hofner & Sparke (1994) showed that settling to this steady-state warped disk structure occurs from the inside, out, and is driven not by dissipative processes that are similar to those which are thought to drive settling in most stellar or protostellar accretion disks but, rather, because “bending waves carry energy associated with transient disturbances out toward the disk edge.” They also showed that, during an evolution as the bending waves propagate outward through the intermediate region of the disk, a twisted structure can develop and persist until the gas has had sufficient time to settle into the steady-state (constant line of nodes) configuration. Sparke & Casertano (1988) and Hofner & Sparke (1994) have demonstrated that, with an appropriate choice of parameters, this model of disk warping matches well the observed properties of several galaxies with warped disks. (See also Kuijken 1991 and Dubinski & Kuijken 1995.)

As Hofner & Sparke (1994) have pointed out, in galaxies with extended H I disks “the outermost gas cannot be expected to form part of a coherent warping mode.” They did not include normal dissipative forces in their simulations and therefore were unable to comment on how such forces might influence the settling process. In this paper, we examine the disk-settling process from the other extreme, ignoring the self-gravity of the gas but introducing an effective

kinematical viscosity into the dynamical equations in order to simulate the effects of dissipative forces. Hence, our effort is complementary to the work of Hofner & Sparke (1994) and is most relevant to galaxies with extended H I disks – although there is one galaxy used for model comparisons (NGC 2841) that is shared by both works. We adopt the view that warps in extended H I disks which exhibit substantial twists are transient features. Independent of precisely what physical process was responsible for initially placing the gas in an orbit that is inclined to the halo’s equatorial plane (*e.g.*, gas infall at the time of formation or a recent tidal encounter with another galaxy), the twisted structure can be understood as the result of differential precession in the gaseous disk as it dissipatively settles toward that “preferred plane.”

In the past, there has been considerable concern (first enunciated by Kahn & Woltjer [1959], but reiterated in the reviews by both Toomre [1983] and Binney [1991]) that differential precession will destroy any warped disk structure on a time scale that is short compared to a Hubble time and, therefore, that the mechanism we are examining cannot reasonably be used to explain the persistence of such structures. In the outermost regions of H I disks, however, precession times are relatively long and, as was first pointed out by Tubbs & Sanders (1979), a warped gas layer can persist for a Hubble time if the dark halo in which the disk is embedded deviates only slightly from spherical symmetry. By modeling carefully the process of disk settling that is driven by normal dissipative forces and comparing the models to the observed kinematical properties of galaxies with extended, warped H I layers, we hope to be able to more carefully examine the viability of such models.

Steiman-Cameron & Durisen (1988, hereafter SCD88) have developed this idea rather extensively. They have adopted a numerical, cloud-fluid model to simulate the time-dependent evolution of a galaxy disk that initially is tilted out of the equatorial plane of an underlying, spheroidal dark halo. The disk is assumed to be composed of a set of annular mass elements, or “clouds,” which act like atoms in a viscous fluid. The SCD88 model has offered some valuable physical insight into the time-dependent settling process that is driven by normal dissipative forces and their dynamically generated model of a twisted galaxy disk has been surprisingly successful at matching the peculiar optical image of one particular galaxy, NGC 4753 (Steiman-Cameron, Kormendy & Durisen 1992).

Our model is analogous to the one developed by SCD88 but it derives from an analytical prescription of the viscous settling process. More specifically, we employ the “twisted-disk” equation formalism first developed by Bardeen & Petterson (1975) and Petterson (1977, 1978) to describe the time-dependent settling of a thin, viscous disk in a nonspherical dark halo potential. This is a rather natural formalism to adopt because, as numerous kinematical “tilted-ring” models have demonstrated, warped H I galaxy disks display a structure that resembles, at least qualitatively, the twisted geometry that had once been thought to be important in accretion disks which surround certain compact stellar objects (Bardeen & Petterson 1975; see a recent rejuvenation of this idea put forward by Maloney & Begelman 1997). In adapting the model to galaxy disks, we have replaced the approximate Keplerian gravitational potential used in earlier

accretion disk work with a logarithmic potential appropriate to galaxy halos. (Pringle [1992] also recently described how the twisted-disk formalism may be adapted to galaxies.) In the limit of stress-free precession, our model reproduces the analytical prescription of disk settling first presented by SCD88, but our model is not constrained to this limit. A more general solution to the governing equations predicts an exponential settling rate that depends on time to the first power, rather than on time to the third power as has been derived in the limit of stress-free precession. Furthermore, an analytical, steady-state solution to the governing equations produces a twisted-disk structure that is very similar to previously constructed, kinematical models. We demonstrate that projected surface density maps and radial velocity maps derived from our analytical model match published H I maps of five well-studied warped disk galaxies (M83, NGC 300, NGC 2841, NGC 5033, and NGC 5055) very well.

## 2. The Generalized Twist-Equation

Bardeen & Petterson (1975) and Petterson (1978) have written the hydrodynamic equations determining the structure and evolution of nonplanar, thin accretion disks in a “twisted-coordinate system.” In this system, the position  $P$  on each ring of radius  $r$  is referenced to a local cylindrical coordinate frame  $(r, \psi, z')$  which has been rotated with respect to the cartesian coordinate system of the central reference ring by the two orientation angles  $\gamma$  and  $\beta$  (see Fig. 1). For an appropriate choice of the two functions  $\gamma(r)$  and  $\beta(r)$ , including specifically the assumption that  $\beta(r) \ll 1$ , the equations separate into a set of the usual hydrodynamic equations for a flat disk and a pair of coupled “twist-equations” governing the orientation of the disk. Because of its ability to describe an apparently complicated, fully three-dimensional dynamical problem with a relatively simple and elegant mathematical model, a number of different groups have subsequently also adopted this formalism. However, until recently there has been some disagreement over what terms may be dropped from the fully three-dimensional, nonlinear partial differential equations (due to their “smallness” relative to other terms) when deriving the governing twist-equations. (For a complete discussion of the various simplifications and assumptions made in deriving this formalism see Petterson [1978, 1979]; Hatchett, Begelman, & Sarazin [1981]; and Papaloizou & Pringle [1983].) As the following brief review points out, the disagreements have not been over the general *form* of the equations but, rather, over the precise value of certain order-unity coefficients. Ultimately, as explained below, we have adopted the derivation presented by Papaloizou & Pringle (1983).

According to Petterson (1978), the twist-equations take the following form:

$$\begin{aligned} \dot{\beta} + v_r \beta' &= \frac{\nu}{2} C_0 \left[ \beta'' + C_1 \frac{\beta'}{r} - \gamma'^2 \beta \right] + \frac{1}{2\pi v_\psi} \int_0^{2\pi} F_T \cos \psi \, d\psi, \\ \dot{\gamma} + v_r \gamma' &= \frac{\nu}{2} C_0 \left[ \gamma'' + C_1 \frac{\gamma'}{r} + \frac{2\gamma' \beta'}{\beta} \right] + \frac{1}{2\pi \beta v_\psi} \int_0^{2\pi} F_T \sin \psi \, d\psi, \end{aligned} \tag{1}$$

with  $C_0 = 2$  and  $C_1 = 1/2$ . In these expressions, dots and primes denote differentiation with

respect to time and space, respectively,  $v_r$  and  $v_\psi$  are the radial and azimuthal components of the fluid velocity,  $\nu$  is the vertically averaged kinematical viscosity, and  $F_T$  is an externally supplied “twisting force”.

Hatchett, Begelman, & Sarazin (1981, hereafter HBS) pointed out some inconsistencies between Petterson’s (1978) derivation and the earlier presentation by Bardeen & Petterson (1975). Through an independent derivation, they determined that the twist-equations do take the form of equation (1), but they concluded that the two coefficients should have the values  $C_0 = 1$  and  $C_1 = -1$ . Most significantly, HBS showed that the pair of twist-equations can be written as a single, *complex* twist-equation of the form

$$\dot{w} + v_r w' = \frac{\nu}{2} C_0 \left( w'' + C_1 \frac{w'}{r} \right) + iL, \quad (2)$$

where the complex variable  $w$  is defined in terms of the angles  $\beta$  and  $\gamma$  as

$$w \equiv (\beta \sin \gamma) - i(\beta \cos \gamma), \quad (3)$$

and

$$L \equiv -\frac{1}{2\pi v_\psi} \int_0^{2\pi} F_T \exp [i(\gamma + \psi)] d\psi. \quad (4)$$

Written in this form, the twist-equation readily submits to analytical solution for certain driving forces.

Papaloizou and Pringle (1983, hereafter PP) have suggested that the HBS derivation also has shortcomings (for example, as viscous evolution occurs according to the HBS equations, angular momentum does not appear to be conserved globally). They have derived a set of twist-equations that more consistently ties in with traditional  $\alpha$ -disk models and have demonstrated explicitly that their derived equations conserve angular momentum. As can most easily be deduced from the presentations of Kumar & Pringle (1985) and Pringle (1992), for a disk whose inner radius goes to zero and whose surface density is independent of radius, the PP derivation also leads to a complex twist-equation that takes the form of equation (2). However, adopting PP’s “naive approach” in order to gain physical insight into the nature of the problem (i.e., setting Kumar and Pringle’s function  $f(\alpha) = \alpha$ ), one concludes from these three papers that the proper coefficients are:

$$C_0 = 1, \quad (5a)$$

$$C_1 = \left[ 2 \frac{d \ln(v_\psi/r)}{d \ln r} + \frac{d \ln Z}{d \ln r} \right], \quad (5b)$$

where

$$Z \equiv r^2 v_\psi. \quad (5c)$$

For a Keplerian disk  $v_\psi \propto r^{-1/2}$ ; therefore,  $C_0 = +1$  and  $C_1 = -3/2$ . Interestingly, these are the same coefficients that appear in Bardeen & Petterson’s (1975) earliest presentation of the twist equations. Henceforth, we will adopt and build upon the twist-equations derived by PP because

it is clear that in a viscous disk evolution that is governed by the PP twist-equations, angular momentum is conserved.

Petterson (1978), HBS, and PP each used an approximately Keplerian potential to represent the underlying gravitational potential well that governs disk dynamics. While the Keplerian potential correctly describes the gravitational field in which a thin accretion disk surrounding a compact object sits, it is inappropriate for a thin galaxy disk sitting in the potential well of a nonspherical dark-matter halo. Utilizing Kumar & Pringle’s (1985) and Pringle’s (1992) extensions of the PP derivation, it is possible to generalize the complex twist-equation to incorporate an arbitrary power-law form for the gravitational potential. Specifically, adopting a rotation law of the form

$$v_\psi \propto r^{(1-q)}, \quad (6)$$

expression (5b) becomes

$$C_1 = \left[ -2q + (3 - q) \right]. \quad (7)$$

Furthermore, as Petterson (1978) has pointed out, the radial velocity can be expressed in terms of the vertically averaged kinematical viscosity as

$$v_r = \nu \frac{r}{v_\psi} \frac{\partial}{\partial r} \left( \frac{v_\psi}{r} \right). \quad (8)$$

Employing our generalized rotation law, we therefore can write

$$v_r = -q \frac{\nu}{r}. \quad (9)$$

Using this expression in conjunction with equations (5a) and (7), the complex twist-equation (2) takes the form:

$$\dot{w} = \frac{\nu}{2} \left[ w'' + (3 - q) \frac{w'}{r} \right] + iL. \quad (10)$$

### 3. Twisted Disks in a Scale-Free Logarithmic Potential

As outlined in § 1, our objective is to examine the evolution of a cold gaseous disk that is embedded in a spheroidal, dark halo potential. In general, we assume that when the gas is initially introduced into the halo potential well, the orientation of its angular momentum vector is not aligned with the symmetry axis of the halo. Because the halo is not spherically symmetric, the halo’s gravitational field will exert a finite “twisting force” on the gaseous disk; in simplest terms, this field forces rings of gas at different radii to precess about the symmetry axis (or symmetry plane) of the halo.

In the present context, a spheroidal dark-matter halo can be satisfactorily represented by a scale-free logarithmic potential (cf. Richstone 1980; Steiman-Cameron & Durisen 1988, 1990).

This potential is a useful approximation because a circular disk orbiting inside such a potential will exhibit a flat rotation curve (i.e.,  $q = 1$  and  $v_\psi$  is independent of radius), as seen in real galaxies. In a halo potential of this type, the precession frequency about the symmetry axis of the potential  $\omega_p$  is

$$\omega_p = \pm \frac{3}{4} \eta \frac{v_\psi}{r}, \quad (11)$$

where  $\eta$  is a constant which measures the strength of the quadrupole distortion of the halo and the minus (plus) sign indicates that the spheroidal halo is oblate (prolate).

For a twisted disk embedded in a spheroidal potential well, the twisting force that enters the derived twist equation assumes precisely the same algebraic form as the twisting force that Bardeen & Petterson (1975) used when modeling the evolution of a disk orbiting a nonspherical, compact stellar object, namely,

$$F_T = 2\omega_p v_\psi \beta \sin \psi. \quad (12)$$

Hence, from equation (4),

$$L = \omega_p w, \quad (13)$$

and we deduce that the evolution of a thin galaxy disk in a scale-free logarithmic halo potential can be described by the expression

$$\dot{w} = \frac{\nu}{2} [w'' + 2\frac{w'}{r}] \pm i \left( \frac{3}{4} \eta v_\psi \right) \frac{w}{r}. \quad (14)$$

Unless explicitly stated otherwise, we henceforth will adopt the minus sign in front of the last term of this expression, thereby assuming that the halo is *oblate* in shape.

Before the character of *general* solutions to this complex ordinary differential equation is examined, it is worthwhile to demonstrate that when certain limiting physical conditions are imposed, familiar analytical expressions for the time variation of the inclination angle  $\beta(t)$  and the “twist” angle  $\gamma(t)$  are derivable from (14). This will give us additional confidence that (14) offers a valid description of the dynamics of a twisted galaxy disk. We present, first, the limit of viscous-free precession, then the limit of stress-free precession.

### 3.1. Viscous-free Precession

In the limit where viscous effects are completely negligible,  $\nu \rightarrow 0$  and equation (14) reduces to the case of free precession,

$$\dot{\gamma} = -\frac{3}{4} \eta \frac{v_\psi}{r} \quad (15a)$$

with no associated evolutionary damping of orbit inclinations, that is,

$$\dot{\beta} = 0. \quad (15b)$$



Equation (15a) can be integrated to give

$$\gamma(r, t) = \gamma_0(r) - \left( \frac{3}{4} \eta \frac{v_\psi}{r} \right) t, \quad (16)$$

where  $\gamma_0(r)$  prescribes the twisting of the disk at time  $t = 0$ .

### 3.2. Stress-free Precession

If the viscous stresses due to twisting have negligible effect on differential precession during the settling process – a condition that SCD88 refer to as “stress-free precession” – one may set  $\beta'' = \gamma'' = \beta' = 0$  in the governing, complex twist-equation. Under this condition, equation (14) predicts the following evolutionary behavior:

$$\dot{\gamma} = \nu \frac{\gamma'}{r} - \frac{3}{4} \eta \frac{v_\psi}{r} \quad (17a)$$

$$\dot{\beta} = -\frac{1}{2} \nu (\gamma')^2 \beta. \quad (17b)$$

This pair of equations matches equations [37a] and [37b] of SCD88 except that the first term on the RHS of equation [17a] is a factor of 2 larger than the equivalent term in equation [37b] of SCD88. We suspect that the SCD88 result is in error, but we have been unable to identify where SCD88 dropped the factor of 2 because their published derivation was not sufficiently clear.

If we furthermore adopt the “stress-free” precession condition introduced by SCD88, the first term in equation (17a) is set to zero (hence the discrepant factor of 2 is not an issue) and the equation reduces to the form of equation (15a) — hence,

$$\gamma' = \gamma'_0 + \left( \frac{3}{4} \eta \frac{v_\psi}{r^2} \right) t. \quad (18)$$

With  $\gamma'_0 = 0$ , equation (17b) specifically integrates to give

$$\beta = \beta_0 \exp \left[ -(t/\tau_e)^3 \right], \quad (19)$$

where

$$\tau_e \equiv \left[ \left( \nu/6 \right) \left( \frac{3}{4} \eta \frac{v_\psi}{r^2} \right)^2 \right]^{-\frac{1}{3}}, \quad (20)$$

and  $\beta_0$  is the value of the inclination at  $t = 0$ . Hence the analytical settling model presented by SCD88 (see also Steiman-Cameron, Kormendy, & Durisen 1992) can be straightforwardly derived from our generalized twist-equation.

It is not at all clear how widely applicable the SCD88 analytical settling model is to the warped H I disks of normal spiral galaxies because the simplifying assumptions (e.g.,  $\beta'' = \gamma'' = \beta' = 0$ ) are quite limiting. However, with the analytical twist-equation in hand, we can perform a less restrictive examination of such systems.

### 3.3. General Separable Treatment

We begin by rewriting equation (14) in the form

$$\dot{w} = w'' + 2\frac{w'}{x} - i\frac{w}{x}, \quad (21)$$

where derivatives are now taken with respect to the dimensionless time and space variables

$$\begin{aligned} \tau &\equiv t/t_0 \\ x &\equiv r/r_0, \end{aligned}$$

and

$$t_0 \equiv \frac{8}{9}\nu(\eta v_\psi)^{-2} \quad (22)$$

$$r_0 \equiv \frac{2}{3}\nu(\eta v_\psi)^{-1}. \quad (23)$$

If we assume that the spatial and temporal parts of the complex angle  $w$  are separable, i.e.,

$$w = T(\tau) \cdot \zeta(x), \quad (24)$$

then

$$T = T_0 \exp[-k^2\tau], \quad (25)$$

where  $k$  is in general complex, and  $\zeta(x)$  must be a solution of

$$\zeta'' + 2\frac{\zeta'}{x} + \left(k^2 - \frac{i}{x}\right)\zeta = 0. \quad (26)$$

The above equation can be transformed by the substitutions  $\xi^2 = -4ix$  and  $\zeta(x) = Z(\sqrt{-4ix})/\sqrt{x}$ , into a form which shows its relationship to Bessel's equation

$$\frac{d^2Z(\xi)}{d\xi^2} + \frac{1}{\xi}\frac{dZ(\xi)}{d\xi} + \left(1 - \frac{1}{\xi^2} - \frac{1}{4}k^2\xi^2\right)Z(\xi) = 0. \quad (27)$$

The character of the solutions and the spectrum of  $k$  are determined by boundary conditions, but some general comments can be made without reference to specific boundary conditions or initial state. The fact that one can do so is important here since we do not have a well-posed problem in which we know the initial state and the relevant boundary conditions. For each  $k$  there is a radius  $x$  inside which the third term inside the parantheses in equation (27) may be neglected. In this region the solution behaves as  $J_1(\xi)$ . We rule out  $Y_1$  because it is not finite at the origin (Abramowicz & Stegun 1972) whereas for plausible initial states  $w$  must be finite everywhere. In general, the spectrum of  $k$  may contain both growing and decaying modes. We do not consider growing modes since their presence would indicate instability. The fact that one can fit a number of observational cases with the simpler solution in which only decaying modes are present may be considered a justification *a posteriori* of this assumption. In any case, it is clear that if an arbitrary

initial state can be written as a superposition containing many values of  $k$  satisfying appropriate boundary conditions, the behaviour in the central region will approach the solution with  $k = 0$ . This tendency manifests itself as a function of time first near the center and later further out as any contribution with large  $Re(k^2)$  dies away rapidly. Since the solution with  $k = 0$  is formally the steady-state solution, we would expect it to apply more or less universally to the interior regions of twisted disks, no matter what the initial conditions were. The memory of the initial conditions is erased inside-out leaving at most an exponentially decaying twist in the innermost regions.

Because the functions of primary interest to us ultimately are  $\beta(x)$  and  $\gamma(x)$ , we note that

$$\beta = T_0 \left[ \zeta_R^2 + \zeta_I^2 \right]^{\frac{1}{2}} \exp \left[ -Re(k^2)\tau \right], \quad (28)$$

$$\gamma = (\theta + \phi) + \frac{\pi}{2}, \quad (29)$$

where:

$$\zeta = \zeta_R + i\zeta_I, \quad (30)$$

$$\theta \equiv -Im(k^2)\tau, \quad (31)$$

$$\phi \equiv \tan^{-1}(\zeta_I/\zeta_R). \quad (32)$$

Because  $\dot{\gamma} = \dot{\theta} = -Im(k^2)/t_0$ , we recognize also that for a given  $k$ , the time-dependent solution of equation (21) presents a wave (with a “twisted” spiral character) that propagates azimuthally through the disk with a pattern speed

$$\Omega_p = -Im(k^2)/t_0 = -\frac{8}{9}Im(k^2)\frac{(\eta v_\psi)^2}{\nu}. \quad (33)$$

### 3.4. Steady-State Solution

Drawing on the HBS discussion, we realize that an analytical solution to the steady-state problem can be derived. Specifically, setting  $\dot{w} = 0$  in equation (21) or  $k^2 = 0$  in equation (27), we obtain formally

$$w = \frac{1}{\sqrt{x}} Z_1[\sqrt{-4ix}], \quad (34)$$

where  $Z_1$  is any first-order Bessel function of the first kind (see Gradshteyn & Ryzhik 1965, §8.491, equation 3). The physically most relevant solution appears to be  $Z_1 = J_1$  because in this case  $\beta$  is finite as  $x \rightarrow 0$  and as  $x$  increases,  $\beta$  increases monotonically (Abramowicz & Stegun 1972). As a point of reference for all subsequent models, then, we define the steady-state twisted-disk function

$$w_{ss} \equiv \frac{1}{\sqrt{x}} J_1[\sqrt{-4ix}] = \frac{1}{\sqrt{x}} [\text{ber}_1(2\sqrt{x}) + i\text{bei}_1(2\sqrt{x})]; \quad (35)$$

where  $\text{ber}_1$  and  $\text{bei}_1$  are the Bessel-real and Bessel-imaginary or Kelvin functions (see e.g. McLachlan 1941; Abramowicz & Stegun 1972). This solution leads to the functions  $\beta_{ss}(x)$  and  $\gamma_{ss}(x)$  shown in Fig. 2. From (35) one can obtain  $\beta_{ss}$  and  $\gamma_{ss}$  in closed form as follows:

$$\beta_{ss} = \frac{1}{\sqrt{x}} M_1(2\sqrt{x}), \quad (36a)$$

$$\gamma_{ss} = \theta_1(2\sqrt{x}) + \frac{\pi}{2}; \quad (36b)$$

where  $M_1(x)$  and  $\theta_1(x)$  are the modulus and phase functions for  $\text{ber}_1(x)$  and  $\text{bei}_1(x)$ . Over the interval  $1 \lesssim x \lesssim 20$ ,  $\beta_{ss}$  and  $\gamma_{ss}$  are approximated well by the expressions:

$$\beta_{ss} \approx 1 + 1.20 \left(\frac{x}{10}\right) + 0.75 \left(\frac{x}{10}\right)^2 + 1.22 \left(\frac{x}{10}\right)^3, \quad (37a)$$

$$\gamma_{ss} \approx \frac{\pi}{4} \left[ 1 + 6.8 \left(\frac{x}{10}\right) - 3.9 \left(\frac{x}{10}\right)^2 + 1.63 \left(\frac{x}{10}\right)^3 - 0.28 \left(\frac{x}{10}\right)^4 \right]. \quad (37b)$$

As we shall illustrate presently, the *form* of the function  $w_{ss}$  over the interval  $1 \lesssim x \lesssim 20$  defines a warped disk model whose features match the observed properties of a number of individual H I disks.

## 4. Application to Galaxies

### 4.1. Standard Model

The steady-state solution just derived is formally inappropriate for real galaxies especially because the outermost regions of real galaxy disks are unlikely to be described well by time-independent conditions. However, over the (innermost) regions of a galaxy disk where differential precession and viscous dissipation have been able to effect appreciable settling in a Hubble time, we expect the spatial structure of the disk to assume a form that is very similar to the one portrayed by the function  $w_{ss}(x)$ . More specifically, the discussion in §3.3 and equations (28)-(32) suggest a general time-dependent behavior of the form:

$$\beta \sim g |w_{ss}|, \quad (38a)$$

$$\gamma \sim \tan^{-1}[-\text{Re}(w_{ss})/\text{Im}(w_{ss})], \quad (38b)$$

where

$$g \sim \beta_0 e^{-\sigma\tau}, \quad (38c)$$

is a spatial constant that describes the amplitude of the warp at a given time and whose time-evolution follows the above form with  $\sigma$  being the lowest  $\text{Re}(k^2)$  compatible with boundary conditions. Again, since we do not have a well-posed problem, all we can say is that whatever restrictions the boundary conditions impose on the spectrum of  $k$ , only the lowest  $\text{Re}(k^2)$  will survive after some time. When comparing our model to the properties of real galaxy disks, we

will treat  $g$  as a free parameter that measures the overall amplitude of a galaxy’s warp and not be immediately concerned about the values of  $\beta_0$ ,  $\sigma$ , or the age of each disk.

The other free parameter that may be adjusted before our twisted disk model is compared to real galaxy disks is  $x_{max} \equiv r_{max}/r_0$ , the radial cutoff to the function  $w_{ss}(x)$  that will correspond to the maximum radial extent  $r_{max}$  of a galaxy’s H I disk. Although  $r_{max}$  can be specified for individual galaxies (see Table 1), the length scale  $r_0$  as defined in equation (23) cannot be specified *a priori* because neither of the physical parameters  $\nu$  or  $\eta$  is known for individual galaxies. Hence, initially it was unclear to us what cutoff radius  $x_{max}$  (*i.e.*, what range  $0 \leq x \leq x_{max}$ ) should be adopted for our model. Fortunately, from previously published tilted–ring models of warped H I disks we were able to determine how rapidly the warp angle  $\beta$  and the twist angle  $\gamma$  vary with radius in real galaxies. More specifically, we measured the “pitch–angles”  $d \ln \beta(x)/d \ln x$  and  $d \ln \gamma(x)/d \ln x$  in several systems, then looked for the range(s) of  $x$  in our steady–state model over which both pitch–angle values occurred simultaneously. We found good matches only when  $x_{max} \sim 10$ , that is, galaxy models which match the observations cannot be produced with values of  $x_{max}$  that are orders of magnitude less than or greater than 10. Previously constructed tilted–ring models also directed the choices of the maximum warping angles  $g$  in our models.

#### 4.2. Comparison with Specific Galaxies

By selecting a single value of  $x_{max}$  (specifically,  $x_{max} = 13$ ) and a rather narrow range of warp amplitudes  $g$ , we have been able to match many of the qualitative features that are frequently seen in the published H I maps of galaxies. For example, using the model parameters identified in Table 1, we have produced the surface brightness maps and radial velocity maps depicted in Fig. 3 for comparison with published maps of the galaxies M83, NGC300, NGC2841, NGC5033 and NGC5055.

Figure 3 actually has been pieced together from five separate frames of a  $> 600$ -frame digital animation sequence in which the viewer “flies around” our model disk, examining it from a variety of different lines of sight. The two angles  $i_o$  and  $t_o$  uniquely define the orientation of the observer’s line of sight with respect to the  $(x, y, z)$  Cartesian coordinate system (see Fig. 1) that is fixed in the body of the galaxy. (When the inclination angle  $i_o = 0^\circ$  or  $360^\circ$ , the galaxy is being viewed face-on with its angular momentum vector pointing directly at the observer; when  $i_o = 90^\circ$ , the galaxy is seen edge-on with its angular momentum vector pointing down. When the azimuthal orientation angle  $t_o = 0$ , the  $+x$  axis is pointing to the right in each image; when  $t_o = 90^\circ$ , the  $-y$  axis is pointing to the right.) In each frame of Fig. 3, the disk is displayed in three different ways: the righthand image is the disk’s projected 2D velocity contour map; the central image is the disk’s projected 2D surface brightness map; and the lefthand image presents a 3D rendering of an isodensity surface that encloses virtually the entire disk. Each of the velocity contour maps and surface brightness maps in Fig. 3 were produced with the 3D radiative transfer routine developed by Vath (1994); each 3D isodensity surface was generated using the IDL imaging package. In the

lefthand image of each frame, the light source reflecting from the disk’s surface originates from the same position as the viewer’s eye. The five frames displayed in Fig. 3 were selected from our animation sequence because they identify observer lines of sight from which our model’s projected 2D maps match well the published maps of the five indicated galaxies.

NGC 2841: To produce the frame of Fig. 3 that is identified as NGC 2841, we set  $g = 1.2 \times 10^{-2}$  in our model disk which corresponds to a maximum warp at the edge of the disk of  $4.5^\circ$ . In Fig. 3, the galaxy’s angular momentum vector is pointed almost directly straight up (the disk is tipped slightly so that the viewer is seeing the “top” side of the galaxy), so velocity contours to the right of the kinematic minor axis are red-shifted and contours to the left are blue-shifted. Our 2D projected surface-brightness and velocity maps should be compared, respectively, with the H I maps published as Figs. 7a and 7b in Bosma (1981). Bosma’s maps have been reprinted here in Fig. 4a. In order to make the relevant comparisons, the observational maps have been rotated counterclockwise approximately  $125^\circ$  in order to properly orient them with respect to our model images. After this rotation has been made, as our 3D rendering illustrates, the southern edge of our model disk is farther away from the observer than is its northern edge; this is consistent with the tilt interpretation one derives from an optical photograph of NGC 2841 and dust obscuration arguments (cf. Plate 14 in Sandage 1961 and Table 3 of CTSC).

The velocity contour map of our model of NGC 2841 displays the same gentle, counter-clockwise twist as the observed H I velocity map. Furthermore, the north-south extensions seen in Bosma’s surface-brightness map of NGC 2841 can be identified with the “leading arm” features that appear in the projected surface-brightness image of our twisted disk model.

M83: To produce the frame of Fig. 3 that is identified as M83, we set  $g = 2.2 \times 10^{-2}$  in our model disk, which corresponds to a maximum warp at the edge of the disk of  $8.3^\circ$ . The model is oriented so that, in Fig. 3, the galaxy’s angular momentum vector is pointed into the page, almost directly away from the observer. (With this orientation, M83’s optically visible spiral arms – cf. Plate 28 in Sandage 1961 – are “trailing” spiral features.) The disk is not being viewed precisely face-on; as displayed in Fig. 3, it is oriented such that, even if the disk were perfectly flat, its upper half would be tipped slightly away from the observer and its lower half toward the observer. As a result of this orientation, velocity contours to the right of the kinematic minor axis are blue-shifted and contours to the left are red-shifted. Our 2D projected surface-brightness and velocity maps should be compared, respectively, with the H I maps published as Figs. 2 and 3 in Rogstad, Lockhart, & Wright (1974; hereafter RLW). RLW’s maps have been reprinted here in Fig. 4b. In order to make the relevant comparisons, the observational maps have been rotated counterclockwise approximately  $180^\circ$  in order to properly orient them with respect to our model images.

The velocity contour map produced by our twisted disk model of M83 displays most of the broad features that appear in the H I velocity map published by RLW. The surface-brightness map published by RLW displays a pair of faint, “leading spiral” arms that are not noticeable in the

image we have produced in Fig. 3 from our model. (The features are actually present in our model at a very low amplitude level and can be enhanced somewhat by adjusting the model parameter  $g$ . See, for example, the tilted–ring model developed by RLW and the model published by CTSC.) Analogous features *are* present in our surface-brightness image of NGC 300, presented below. As the 3D isodensity surface of our model of M83 suggests, these spiral–arm features probably appear in projected surface-brightness maps of M83 because the galaxy’s twisted H I disk is bending toward the observer in the northwestern quadrant and away from the observer in the southwestern quadrant.

NGC 5033: To produce the frame of Fig. 3 that is identified as NGC 5033, we set  $g = 3.2 \times 10^{-2}$  in our model disk which corresponds to a maximum warp at the edge of the disk of  $12^\circ$ . In Fig. 3, (see also Fig. 5 and the related discussion in §4.3, below), the galaxy’s angular momentum vector is pointed down and away from the observer, so velocity contours to the right of the kinematic minor axis are blue-shifted and contours to the left are red-shifted. Our 2D projected surface-brightness and velocity maps should be compared, respectively, with the H I maps published as Figs. 4a and 4b in Bosma (1981). Bosma’s maps have been reprinted here in Fig. 4c. In order to make the relevant comparisons, the observational maps have been rotated counterclockwise approximately  $100^\circ$  in order to properly orient them with respect to our model images.

Both the velocity contour image and the surface-brightness image produced by our model of NGC 5033 bear a striking resemblance to Bosma’s published maps. The relatively steep density gradients that are visible at the northeast and southwest edges of Bosma’s surface-brightness maps are, according to our model, clearly due to the disk bending toward the observer at one edge and away from the observer at the other.

NGC 5055: To produce the frame of Fig. 3 that is identified as NGC 5055, we set  $g = 5.7 \times 10^{-2}$  in our model disk which corresponds to a maximum warp at the edge of the disk of  $21.3^\circ$ . This galaxy’s angular momentum vector, like that of NGC 5033 (notice that  $i_o$  is the same in these two systems), is pointed down and away from the observer, so velocity contours to the right of the kinematic minor axis are blue-shifted and contours to the left are red-shifted. Our 2D projected surface-brightness and velocity maps should be compared, respectively, with the H I maps published as Figs. 6a and 6b in Bosma (1981). These maps are reprinted in Fig. 4d of this manuscript. In this case, the observational maps did not need to be rotated more than  $\sim 10^\circ$  clockwise in order to make the relevant comparisons.

Again, the velocity contour image and the surface-brightness image produced by our model bear a strong resemblance to Bosma’s published maps. Notice, in particular, that from this line-of-sight, thin arcs are displayed in the upper lefthand and lower righthand regions of our model’s projected surface-brightness map. Bosma’s H I surface-brightness map definitely displays similar features.

NGC300: To produce the frame of Fig. 3 that is identified as NGC300, we set  $g = 5.7 \times 10^{-2}$  in our model disk, which corresponds to a maximum warp at the edge of the disk of  $21.3^\circ$ . The

model is oriented so that the galaxy’s angular momentum vector is pointed out of the page, almost directly at the observer. The disk is not being viewed precisely face-on; as displayed in Fig. 3, it is oriented such that, even if the disk were perfectly flat, its upper half would be tipped slightly toward the observer and its lower half away from the observer. As a result of this orientation, velocity contours to the right of the kinematic minor axis are blue-shifted and contours to the left are red-shifted. Our 2D projected surface-brightness and velocity maps should be compared, respectively, with the H I maps published as Figs. 1 and 2 in Rogstad, Crutcher, & Chu (1979; hereafter RCC). RCC’s maps have been reprinted here in Fig. 4e. In order to make the relevant comparisons, the observational maps have been rotated counterclockwise approximately  $160^\circ$  in order to properly orient them with respect to our model images. Notice that after this rotation has been made, our 3D rendered image of NGC300 closely resembles the perspective drawing of RCC’s tilted-ring model (see their Fig. 6).

Notice, first, that the velocity contour image of our model of NGC 300 closely resembles RCC’s published velocity map. In addition, our surface-brightness map displays a pair of faint, “leading spiral” arms that touch the left and right edges of the image shown in Fig. 3. We believe that these arms provide an explanation for the faint features that extend to the northwest and, particularly, southeast regions of the RCC map.

### 4.3. Prograde versus Retrograde Precession

The model that was used to generate images for Fig. 3 was constructed assuming that the precessional frequency  $\omega_p$  was negative (see eq. 11). That is, the underlying halo was assumed to be *oblate* in shape and accordingly, the precessional motions retrograde with respect to the orbital motion of the gas. Because the magnitude of the precessional frequency *decreases* with increasing radius in each disk, retrograde precession results in a physical twist that has a “leading” appearance in the 3D, rendered image of each system. (In contrast, optically visible spiral arms are generally thought to be “trailing” features.) Knowing this, one can discern whether the angular momentum vector of each galaxy is pointing into (out of) the page by simply noticing whether the warped structure exhibits an overall clockwise (counterclockwise) twist.

As CTSC pointed out, an identically good fit to the H I maps can be obtained with a disk that exhibits a retrograde twist (i.e., one that settles into a prolate spheroidal halo) as with a disk that exhibits a prograde twist. After switching the sign of  $\omega_p$  in eq. (11) to reverse the sense of the twisting in the 3D model, one need only adjust one’s line-of-sight viewing angle according to the prescription

$$i_o' \equiv \pi - i_o \tag{39}$$

$$t_o' \equiv \pi - t_o \tag{40}$$

in order to generate projected velocity and surface-density maps from a “prolate” model that are



identical to the maps generated from an “oblate” model. Fig. 5b illustrates what the “prolate” model for NGC 5033 looks like once this transformation is employed.

If two quite different 3D disk structures (one with a prograde twist and one with a retrograde twist) can generate identical 2D maps when projected onto the sky, how can one decipher which offers the physically more realistic model? As CTSC pointed out, information gleaned from optical photographs can often provide the supplementary information that is needed to identify which model is more realistic. For example, one must insist that the angular momentum vector of M83 points away from the observer (*into* the page on Fig. 3) if its optical spiral arms are to be interpreted as *trailing* features; hence a warped disk model with a prograde twist (and settling in an *oblate* spheroidal halo) as illustrated in Fig. 3 is the preferred solution. Similar arguments (or ones based on dust obscuration) lead one to conclude that the disks of NGC 2841, NGC 5055 <sup>3</sup>, and NGC 300 are also settling in oblate spheroidal halos. However, for NGC 5033, the retrograde twisting (prolate spheroidal halo) model is clearly preferable to the prograde twisting model. This statement is supported by two arguments: first, dust obscuration in an optical photograph of NGC 5033 (cf. Fig. 4a of CTSC and Panel 127 of Sandage & Bedke 1994) identifies the western edge of the galaxy as nearer to the observer than its eastern edge; second, model 5b must be chosen over 5a if the optical spiral arms are to be interpreted as trailing features. Hence, the 3D image of NGC 5033 shown in Fig. 5b is the correct depiction of the galaxy as inferred from our model fitting.

#### 4.4. Interpretation

##### 4.4.1. Limited Range of Model Parameters

It should be noted that the animation sequence from which the frames shown in Fig. 3 were selected was originally constructed with the expressed intention of flying through lines of sight that we previously had determined would produce good fits to M83, NGC 5033 and NGC 300; the only intrinsic model parameter that was adjusted during the fly-by sequence was the overall warp amplitude  $g$ . During our viewing of the fly-by sequence, we also spotted images that matched the published observational maps of NGC 2841 and NGC 5055. The frames presented in Fig. 3 have been taken directly from the original animation sequence; absolutely no attempt has been made to fine-tune the model parameters to fit these two additional galaxies separately. Clearly, then, it is primarily the line-of-sight viewing angle to each disk and not the parameters defining the underlying structural properties of each disk that had to be adjusted from galaxy to galaxy in order to match the observations. Considering its simplicity – in particular, the significantly reduced number of free parameters as compared to previous tilted-ring models – the agreement between the projected maps of our model and observed H I maps is excellent. We conclude,

---

<sup>3</sup>In our judgement, CTSC misidentified NGC 5055 as requiring a prolate halo.

therefore, that the function  $w_{ss}(x)$  and the corresponding expressions for  $\beta_{ss}$  and  $\gamma_{ss}$  given by Eqs. (36a) and (36b) provide a good template for matching the observed kinematical structure of H I disks. Because a single value of the parameter  $x_{max}$  and little variation in the parameter  $g$  are required to achieve a good model fit to five separate galaxies, we conclude that these five systems intrinsically have very similar warped disk structures.

#### 4.4.2. Physical Interpretation

Most importantly, however, since the function  $w_{ss}(x)$  derives from a physically reasonable dynamical picture of disk settling, there is an expectation that our model provides insight into the underlying physical properties of these systems. For example, since  $x_{max} = 13$  for each galaxy, we conclude from definition (23) that in each galaxy, the ratio

$$\frac{\nu}{\eta} \approx 0.12 v_{\psi} r_{max} \sim 600 \text{ km s}^{-1} \text{ kpc} = 2 \times 10^{29} \text{ cm}^2 \text{ s}^{-1},$$

where  $r_{max}$  is the outer radius of the observed H I disk. (Table 1 shows the values of  $\nu/\eta$  calculated individually for each modeled system.) Also, if our model is relevant at all, the existence of each warped layer indicates that viscous settling has been effective in a Hubble time ( $t \sim H_0^{-1}$ ) and  $\tau \sim 1/\sigma$ . Without a proper understanding of the boundary conditions, we are unable to determine the correct physical value of  $\sigma$ . Assuming for the moment that  $\sigma \sim 1$  and setting  $H_0 = 75 \text{ km s}^{-1} \text{ Mpc}^{-1}$ , we conclude from definition (22) that

$$\frac{\nu}{\eta^2} \sim v_{\psi}^2 H_0^{-1} \sim 600 \text{ km s}^{-1} \text{ Mpc}.$$

These two ratios can only hold if, in each system,

$$\nu \sim 0.6 \text{ km s}^{-1} \text{ kpc} = 2 \times 10^{26} \text{ cm}^2 \text{ s}^{-1}$$

and

$$\eta \sim 10^{-3}.$$

It is worth noting that the values obtained for  $\nu$  in all cases (see Table 1) are consistent with a rough estimate of the viscosity due to dissipational cloud–cloud collisions in the solar neighborhood where  $\nu \sim 0.25 \text{ km/s kpc}$  (Lynden-Bell & Pringle 1974). Very modest variations in cloud dimensions, r.m.s. velocity and filling factor from galaxy to galaxy are sufficient to reproduce the range of values shown on Table 1. The fact that reasonable viscosity estimates are obtained by assuming  $\sigma \sim 1$  may be considered as a posteriori justification for our choice.

## 5. Discussion and Conclusions

Utilizing the formalism originally introduced by Petterson to describe warped and twisted accretion disk structures in Keplerian potentials, we have derived a single, complex ODE to

describe time dependent settling of an H I disk in the logarithmic potential that appears to be typical of normal spiral galaxies. Over the interval  $1 \lesssim x \lesssim 20$ , the analytical function  $w_{ss}(x)$  – derived from an analysis of the steady-state limit of the general twisted-disk equation – appears to describe quite accurately the general warped and twisted structure that is exhibited by a number of galaxy disks. It should be noted again that our analysis is based on the assumption that the warping angle  $\beta$  is  $\ll 1$ . For galaxies with larger warps (including some that we have modeled) this is a simplifying assumption and should be disregarded in more proper treatments (see Pringle [1992]).

From our model fits we conclude that, quite generally, the effective kinematical viscosity in these neutral hydrogen disks is  $\nu \sim 0.6 \text{ km s}^{-1} \text{ kpc}$ . That is, the effective Reynolds number in these systems is

$$R_e \sim \frac{r_{max} v_\psi}{\nu} \sim \frac{x_{max}^2 v_\psi}{r_{max}} \sim 6000 .$$

According to equation (9), this also implies that the ratio of the radial inflow velocity of the gas to its orbital velocity is

$$\frac{v_r}{v_\psi} \approx \frac{1}{R_e} \sim \times 10^{-4} .$$

This model also provides a mechanism by which the parameter  $\eta$  – the quadrupole moment of the underlying dark halo potential well – can be measured in spiral galaxies. Our fits to five normal spirals with well-studied warped H I disks specifically indicate that  $\eta \sim 10^{-3}$ . (This value can be increased to  $\eta \sim 10^{-2}$ , with a corresponding factor of ten increase in viscosity, only if the age of these disks is assumed to be  $0.1 H_0^{-1}$  – which seems unlikely – or  $\sigma$  in expression 38c is found to be  $\sim 0.1$ .) Hence, we conclude that the dark halos in which these warped disks sit are, to quite high accuracy, spherically symmetric. This particular conclusion should not come as a surprise because some time ago Tubbs and Sanders (1979) pointed out that if warped disks are identified as transient structures, the warp can only be sustained for a Hubble time if the underlying halo potential is very nearly spherical. Although we have examined in detail here only the steady-state solution, the derived time-dependent twisted-disk equation provides a tool that can be utilized to model the time-evolution of warped H I disks without resorting to elaborate numerical techniques.

The twisted-disk formalism in general – and the analytical function  $w_{ss}(x)$  in particular – provides an avenue through which models of warped H I disks can advance from purely kinematical fits (e.g. tilted-ring models) to dynamical models based on a reasonable physical model. In the future, we also expect to use the time-dependent form of the twisted-disk equations as a point of comparison for fully three-dimensional gas dynamic simulations of H I disks settling into distorted halo potentials.

We appreciate the assistance that H. Cohl provided us in rendering the 3D galaxy images shown in Figs. 3 and 5, and also would like to thank Dr. A. Bosma and Dr. D. Rogstad for

granting permission to reprint figures from their earlier papers. We also would like to thank the anonymous referee for suggestions that resulted in substantial improvements in this manuscript. This work has been supported in part by NASA through grants NAGW-2447 and NAG5-2777, and in part by the U.S. National Science Foundation through AST-9528424.

## REFERENCES

- Abramowicz, M. & Stegun, I. A. 1972, *Handbook of Mathematical Functions* (New York: Dover)
- Bardeen, J. M., & Petterson, J. A. 1975, *ApJ*, 195, L65
- Bertin, G., & Mark, J. W.-K. 1980, *A&A*, 88, 289
- Binney, J. 1981, *MNRAS*, 196, 455
- Binney, J. 1992, *ARA&A*, 30, 51
- Bosma, A. 1981, *AJ*, 86, 1791
- Bosma, A. 1991, in *Warped Disks and Inclined Rings Around Galaxies*, eds. S. Casertano, P. D. Sackett, and F. H. Briggs, (New York: Cambridge Univ. Press), 181
- Briggs, F. H. 1990, *ApJ*, 352, 15
- Christodoulou, D. M., Tohline, J. E., & Steiman-Cameron, T. Y. 1993, *ApJ*, 416, 74 (CTSC)
- Dekel, A., & Shlosman, I. 1983, in *Internal Kinematics and Dynamics of Galaxies*, ed. E. Athanassoula, (Boston: Reidel), 187
- Dubinski, J., & Kuijken, K. 1995, *ApJ*, 442, 492
- Gradshteyn, I. S., & Ryzhik, I. M. 1965, *Table of Integrals, Series, and Products* (New York: Academic Press)
- Hatchett, S. P., Begelman, M. C. & Sarazin, C. L. 1981, *ApJ*, 247, 677
- Hofner, P., & Sparke, L. S. 1994, *ApJ*, 428, 466
- Hunter, C., & Toomre, A. 1969, *ApJ*, 157, 183
- Kahn, F. D. & Woltjer, L. 1959, *ApJ*, 130, 705
- Kuijken, K. 1991, *ApJ*, 376, 467
- Kumar, S. & Pringle, J. E. 1985, *MNRAS*, 213, 435
- Lynden-Bell, D. & Pringle, J. E. P. 1974, *MNRAS*, 168, 603

- McLachlan, N. W. 1941, *Bessel Functions for Engineers* (London: Oxford Univ. Press)
- Maloney, P. R. & Begelman, M. C. 1997, *ApJ*, 491, L43
- Newton, K. 1980a, *MNRAS*, 191, 169
- Newton, K. 1980b, *MNRAS*, 191, 615
- Papaloizou, J. C. B., & Pringle, J. E. 1983, *MNRAS*, 202, 1181
- Petterson, J. A. 1977, *ApJ*, 214, 550
- Petterson, J. A. 1978, *ApJ*, 226, 253
- Pringle, J. E. 1992, *MNRAS*, 258, 811
- Reakes, M. L., & Newton, K. 1978, *MNRAS*, 185, 277.
- Richstone, D. O. 1980, *ApJ*, 238, 103
- Rogstad, D. H., Crutcher, R. M., & Chu, K. 1979, *ApJ*, 229, 509
- Rogstad, D. H., Lockhart, I. A., & Wright, M. C. H. 1974, *ApJ*, 193, 309
- Sandage, A. 1961, *The Hubble Atlas of Galaxies* (Washington, D. C.: Carnegie Institute of Washington)
- Sandage, A., & Bedke, J. 1994, *The Carnegie Atlas of Galaxies*, (Washington, D. C.: Carnegie Institute of Washington), vol. 1
- Schwarz, U. J. 1985, *A&A*, 142, 273
- Sparke, L. S. 1986, *MNRAS*, 219, 657
- Sparke, L. S., & Casertano, S. 1988, *MNRAS*, 234, 873
- Steiman-Cameron, T. Y. & R. H. Durisen 1988, *ApJ*, 325, 26
- Steiman-Cameron, T. Y. & R. H. Durisen 1990, *ApJ*, 357, 62
- Steiman-Cameron, T. Y., Kormendy, J., & Durisen, R. H. 1992, *AJ*, 104, 1339
- Toomre, A. 1983, in *Internal Kinematics and Dynamics of Galaxies*, ed. E. Athanassoula, (Boston: Reidel), 177
- Tubbs, A. D. & Sanders, R. H. 1979, *ApJ*, 230, 736
- Väth, H. M. 1994, *A&A*, 284, 319

### FIGURE CAPTIONS

Fig. 1.– The twisted coordinate system. The position  $P$  on each ring of radius  $r$  is referenced to a local cylindrical coordinate frame  $(r, \psi, z')$  which has been rotated with respect to the cartesian coordinate system  $(x, y, z)$  of the central reference ring by the two orientation angles  $\gamma$  and  $\beta$ . (adapted from Petterson 1977)

Fig. 2.– The steady–state behaviors of (a) the inclination angle  $\beta$  and (b) the twisting angle  $\gamma$  in terms of the dimensionless space variable  $x$ .

Fig. 3.– Models of the five galaxies NGC2841, M83, NGC5033, NGC5055, and NGC300, based on the steady–state solution of the complex twist–equation. In each frame, the lefthand image is a 3D isodensity surface which encompasses virtually the entire disk; the central image is the projected 2D surface brightness map of the disk; and the righthand image is the projected 2D velocity contour map of the disk.

Fig. 4.– Observational H I maps of five galaxies are reprinted here for comparison with the models shown in Fig. 3. As detailed in the text, each of these maps has been rotated in order to properly orient it with respect to the corresponding model image. Observed surface brightness and velocity contour maps appear on the left and right, respectively, of each panel (a)-(e). (a) Maps of NGC 2841 (Bosma 1981); (b) maps of M83 (RLW); (c) maps of NGC 5033 (Bosma 1981); (d) maps of NGC 5055 (Bosma 1981); and (e) maps of NGC 300 (RCC).

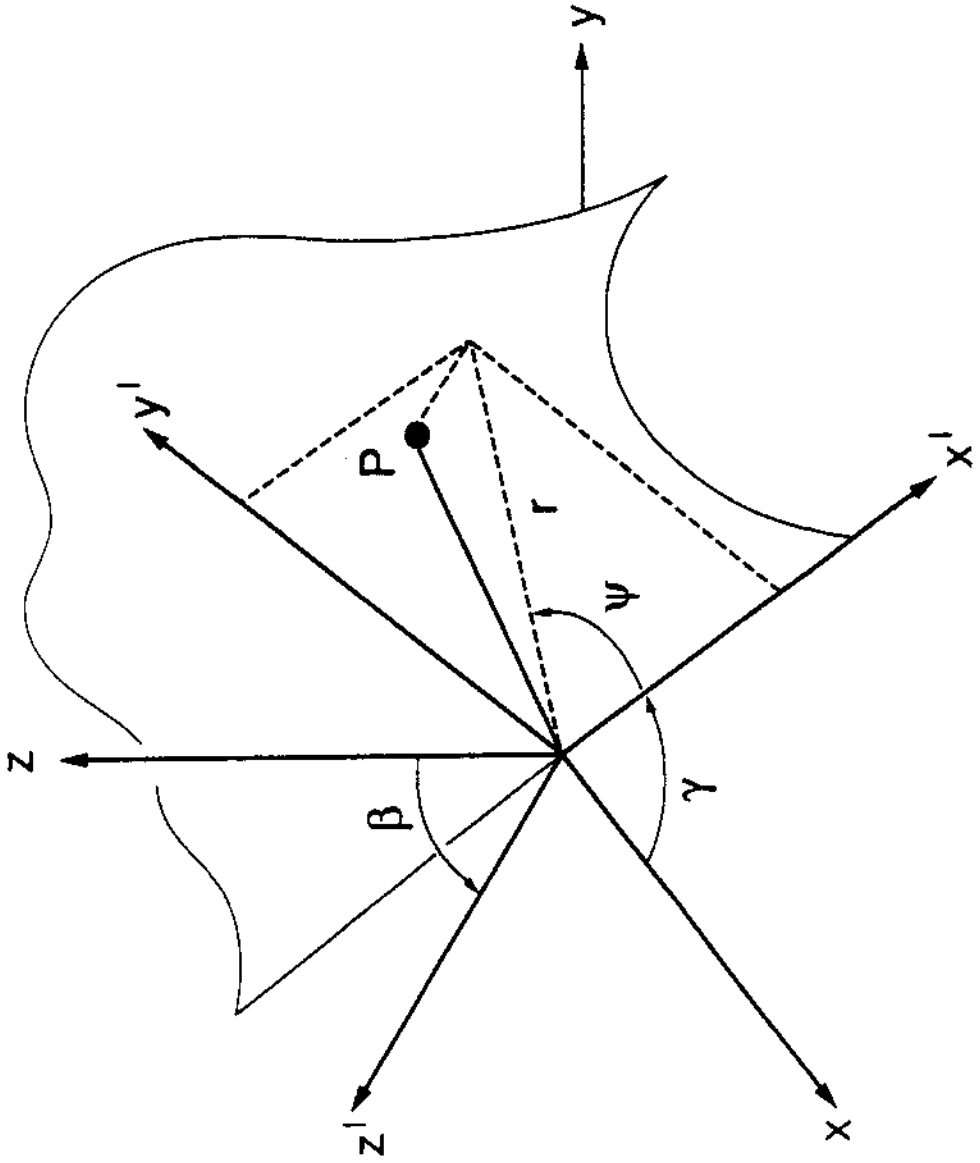
Fig. 5.– 3D isodensity surfaces for the (a) “oblate” and (b) “prolate” models of NGC5033.

Table 1: Model Parameters

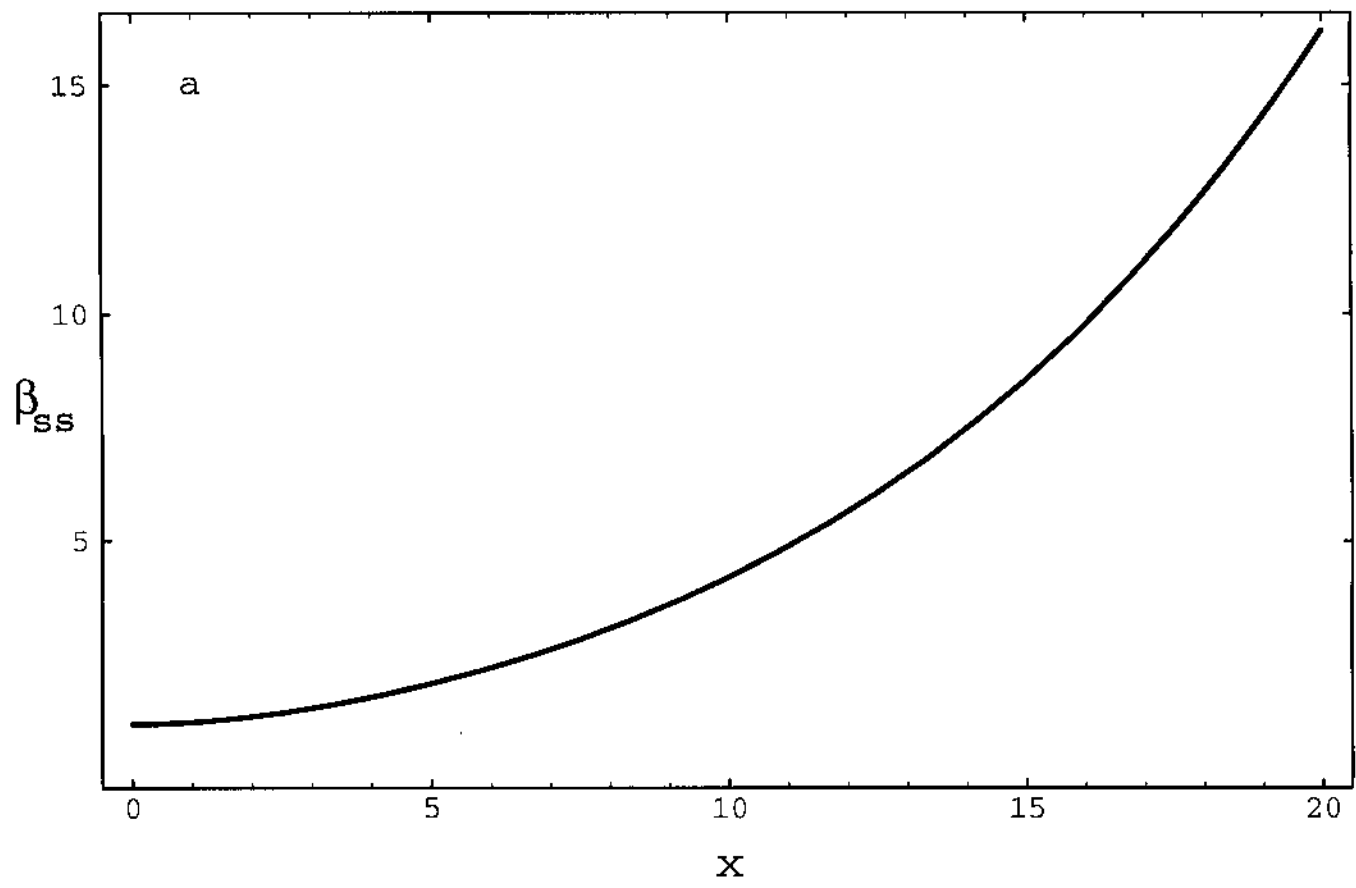
Galaxy	$r_{\max}^a$ (kpc)	$v_{\psi}^a$ (km s <sup>-1</sup> )	$x_{\max}$	$g$	$\beta_{\max}$ (°)	$\nu/\eta$ (km s <sup>-1</sup> kpc)	$\nu$ (km s <sup>-1</sup> kpc)	$\eta$ 10 <sup>-3</sup>
NGC2841	32	300	13	1.2E-2	4.5	1100	1.0	0.92
M83	23	180	13	2.2E-2	8.3	480	0.53	1.1
NGC5033	24	220	13	3.2E-2	12.0	610	0.58	0.94
NGC5055	28	213	13	5.7E-2	21.3	690	0.78	1.1
NGC300	15	94	13	5.7E-2	21.3	160	0.22	1.4

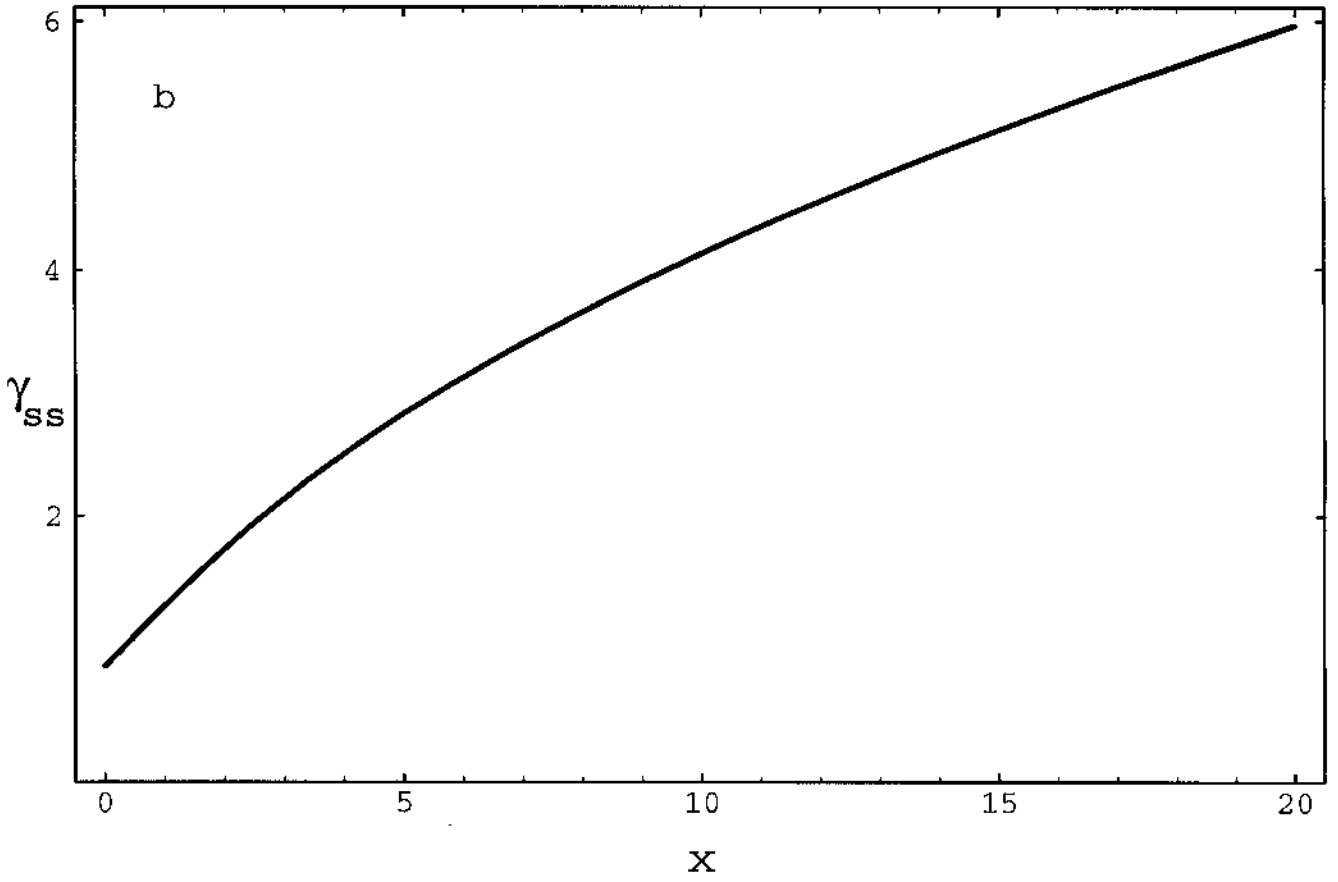
---

<sup>a</sup>From CTSC









$$i_0 = +284^\circ \quad t_0 = +240^\circ$$



NGC 2841

$$i_0 = +174^\circ \quad t_0 = +277^\circ$$



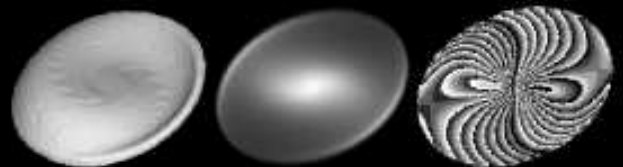
M83

$$i_0 = +125^\circ \quad t_0 = +289^\circ$$



NGC 5033

$$i_0 = +125^\circ \quad t_0 = +435^\circ$$

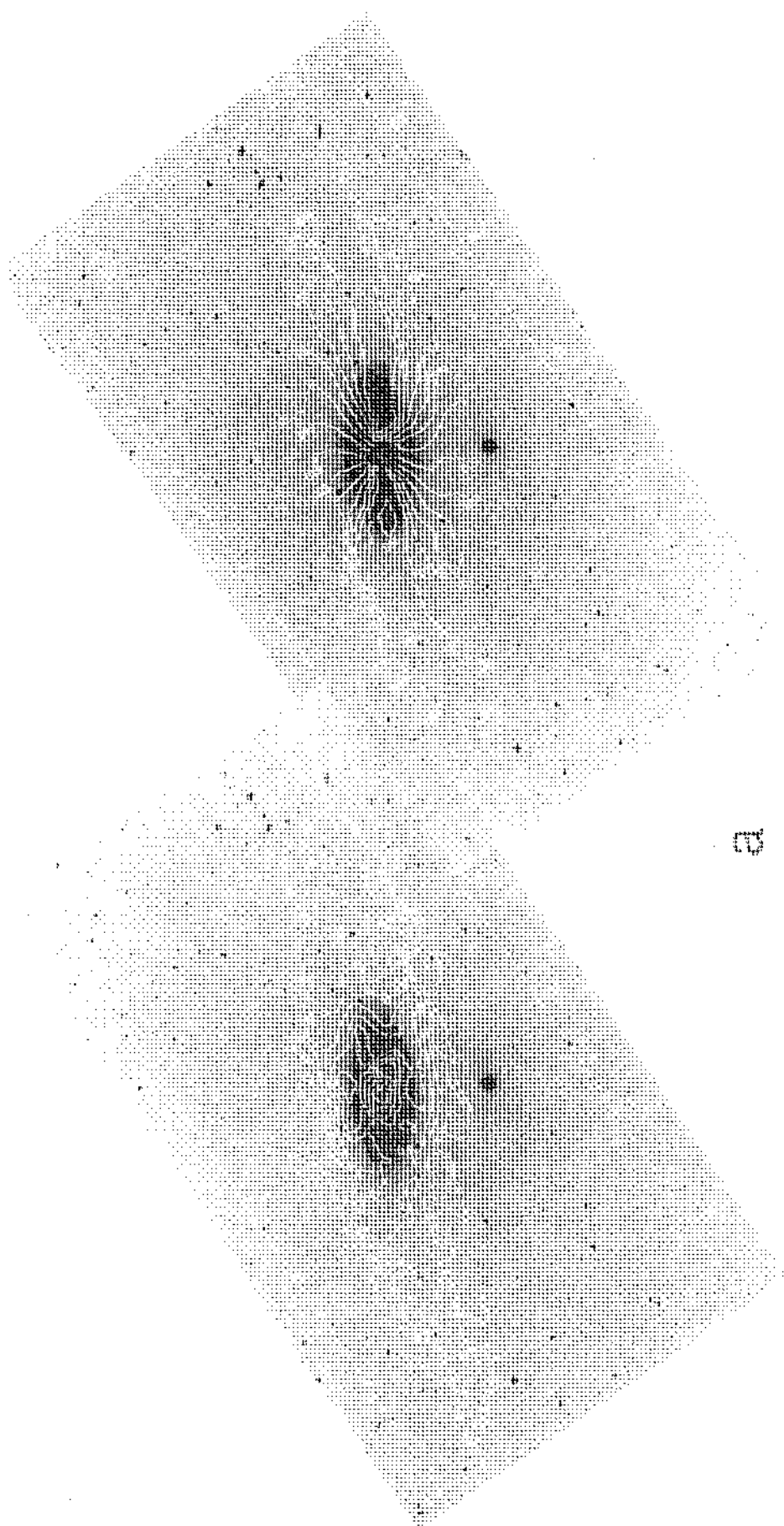


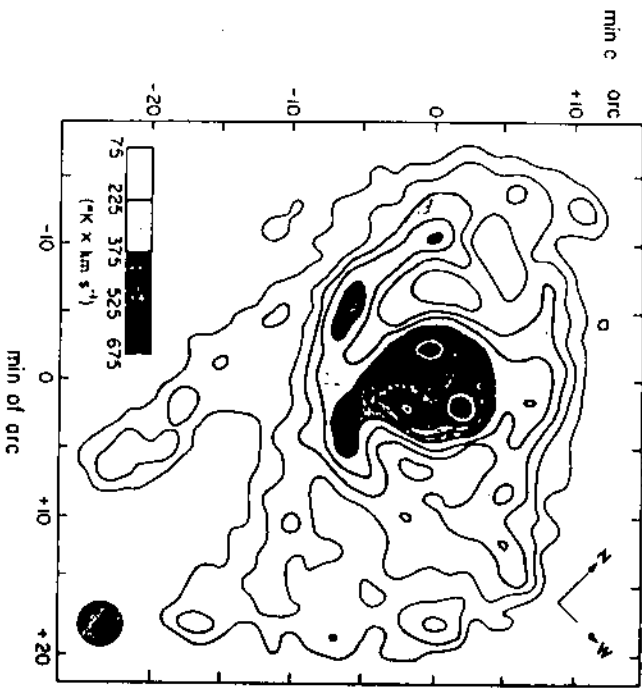
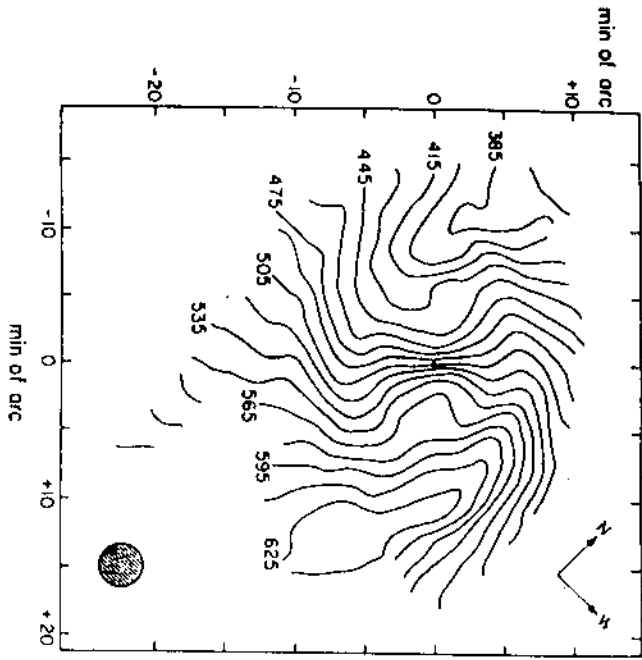
NGC 5055

$$i_0 = +013^\circ \quad t_0 = +469^\circ$$

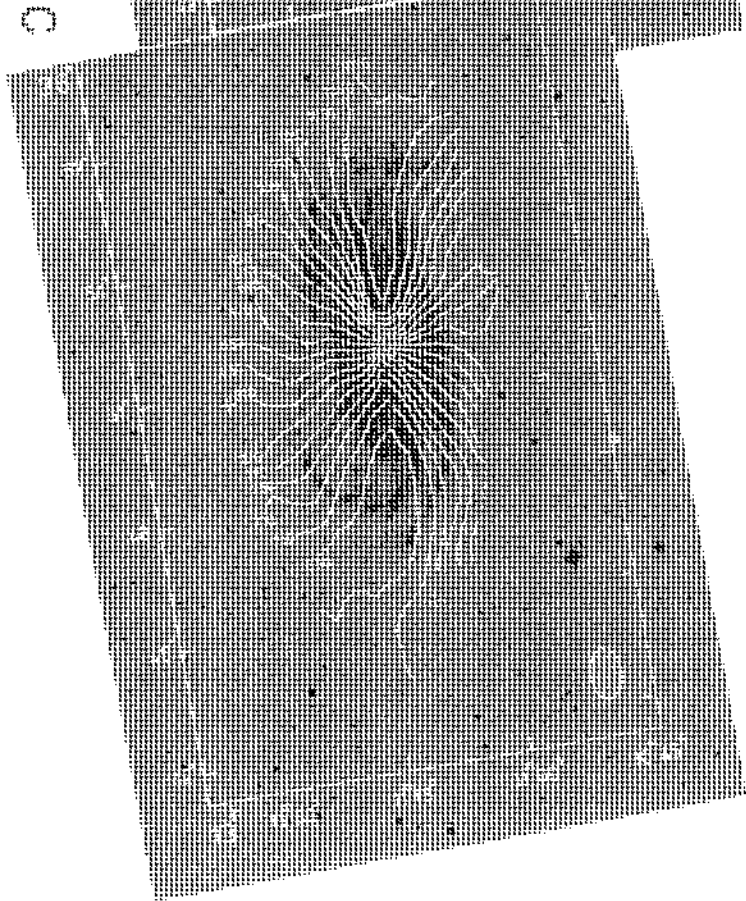
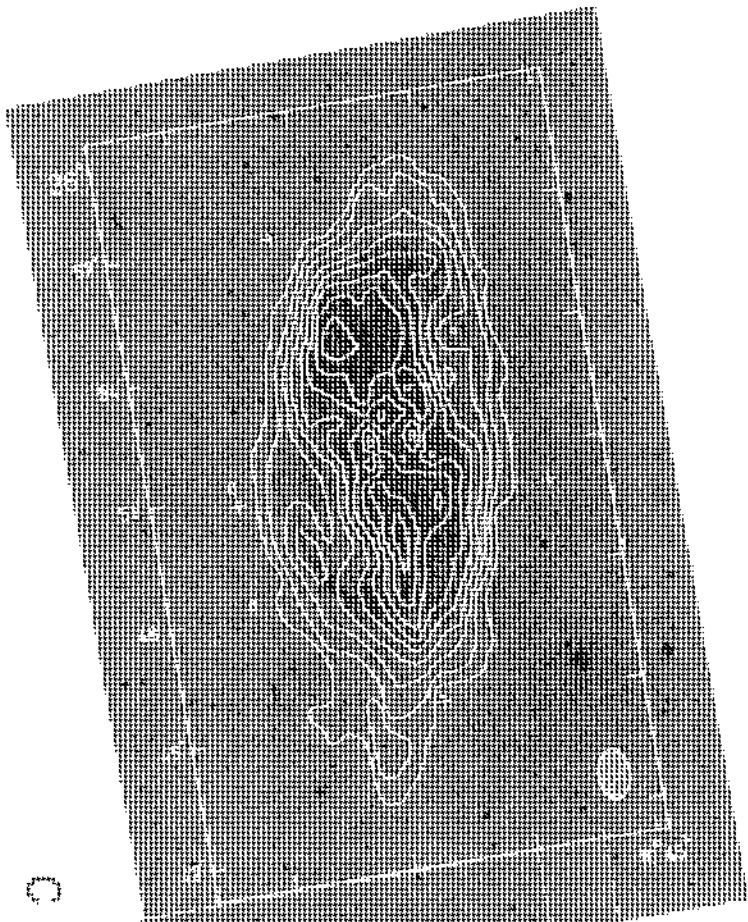


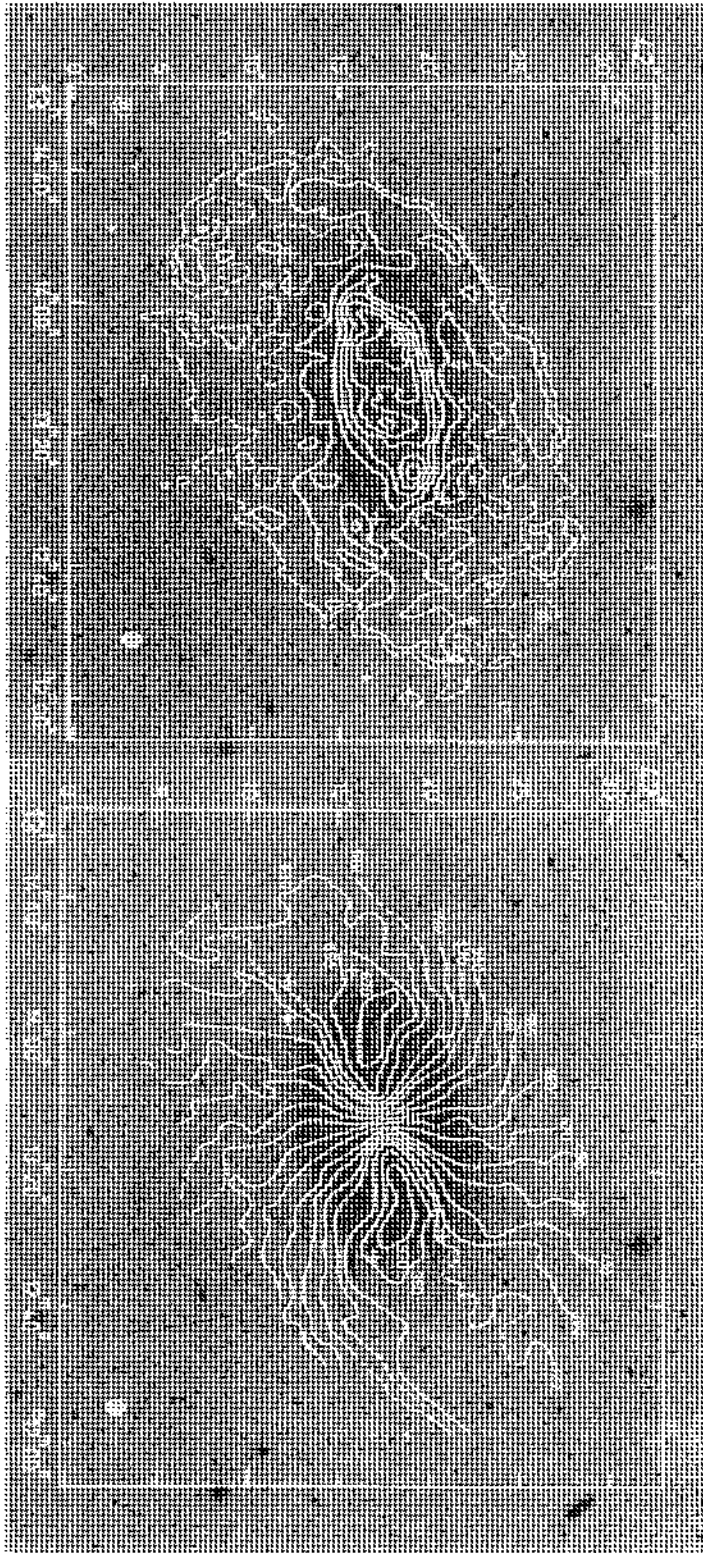
NGC 300



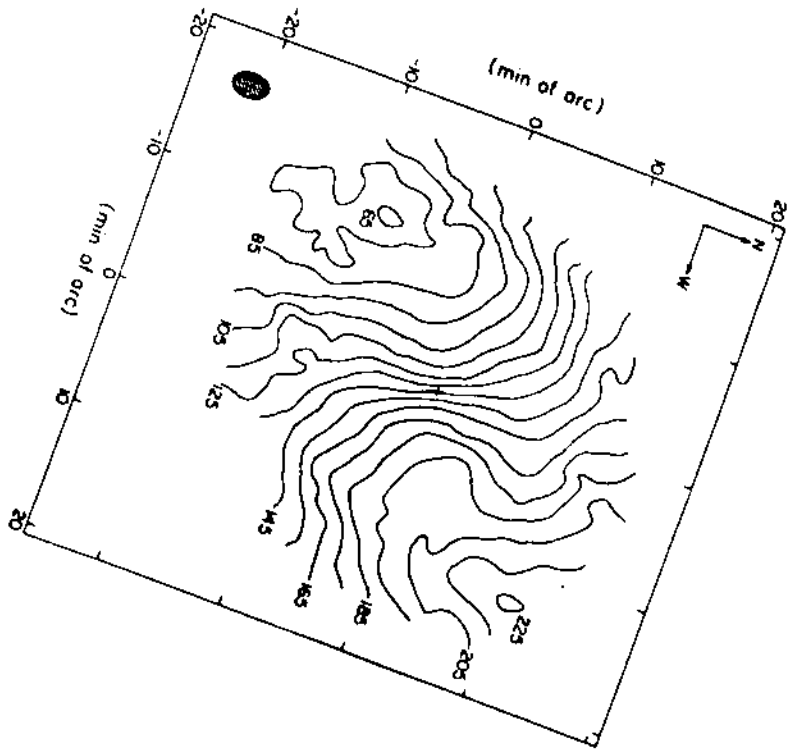


q

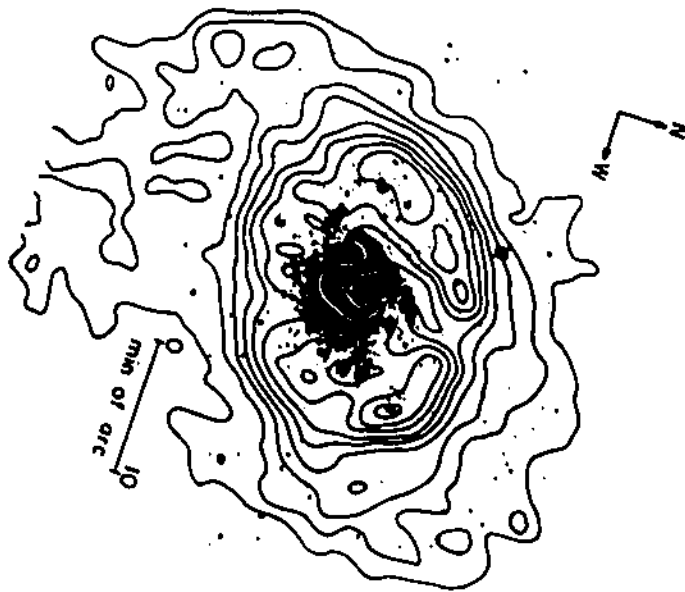




Q



e





$i_o = 125^\circ$   
 $t_o = 289^\circ$



(a)

$i_o = 55^\circ$   
 $t_o = 251^\circ$



(b)

NGC 5033